Optimization of acquisition patterns for establishing inter CubeSat optical communications

René Rüddenklau[1],* ⓘ and Georg Schitter[2] ⓘ

[1]*Institute of Communications and Navigation, Optical Satellite Links, German Aerospace Center (DLR), 82234 Weßling, Germany*
[2]*Automation and Control Institute (ACIN), TU Wien, Gußhausstraße 27-29, 1040 Wien, Austria*
*rene.rueddenklau@dlr.de

As commercially available CubeSats with up to six standardized units cannot achieve the precision required for an instantaneous establishment of a low-divergence optical inter-satellite link, search patterns are used to scan the remaining field of uncertainty. This analysis optimizes the simultaneously executed search pattern combinations of the two laser communication terminals involved. Based on a Monte Carlo simulation, the perturbations on these links are investigated, and the corresponding key performance parameters such as mean acquisition time and success rate are calculated. The results are penalized by the hardware specifications, including actuator and sensor bandwidths, given by their design. Residual attitude error components imply a significant influence on the acquisition process and are therefore presented within this work. The pattern pairs are fed through an automated optimization algorithm to tune and analyze them. In this particular scenario of two CubeISL models, the mean duration for a first detected acquisition hit is within a pattern period of 3.2 s for the best performing pairs *spiral-rose* and *lissajous-rose*. Assuming an uncertainty field of ±0.2 deg due to limited attitude knowledge, success rates between 82.3% and 99.9% are achieved.

1. INTRODUCTION

Optical free-space communication is characterized by high transmission rates. However, this also means that the divergence of the beam should be very low in order to make the best use of the available emitted optical power on a CubeSat. At the same time, this leads to increased pointing accuracy requirements for the entire spacecraft attitude control system, including the fine pointing assembly of the optical terminal. In particular, during the acquisition phase, when optical signals are temporarily unavailable, precise attitude knowledge is essential. Since no high-speed data exchange can take place during the initial acquisition phase, it is therefore an important requirement to reduce the time from the commissioning of the laser communication terminal (LCT) to an established link. Approaches to optimize this task already exist. Which type of search pattern can be used most effectively has been investigated [1]. Analytical approaches have also been proposed, and metrics such as mean acquisition time and success probability have been introduced [2–4]. Furthermore, it has been investigated to what extent external disturbances affect the process, which requires a statistical evaluation [5,6]. Related work has been carried out on small satellites, comparing a *Spiral* and

a *Meander* search pattern. Upon closer examination, none of the mentioned works investigates the case of two CubeSats with 6 units in size, where each unit equals a cube with an edge length of 100 mm. Further, it includes implicit bandwidth constraints imposed by the mechatronic devices used, such as fast steering mirror (FSM) and attitude control systems, in combination with a pattern-based optimization approach.

The main contribution of this work is the analysis of acquisition patterns for an optical inter-satellite link (ISL) by optimizing the probability of success and the expected acquisition time duration, considering the dynamics of the involved system components. The best performing combination of acquisition patterns with respect to a metric will be selected. The design of an acquisition scheme including the baseline pattern *Spiral* and *Grid* has already been considered for a preliminary analysis [7]. However, this work did not include detailed consideration of the perturbations, but was oriented towards a feasible concept. The following work will focus on the first acquisition hit. This is the most critical event in the acquisition phase, as it contains information about the attitude with respect to the counterpart terminal. Consider that, due to the acquisition scheme (cf. Fig. 1), additional time is required

after the first hit occurred to achieve a bidirectional link. The optimization algorithm proposed in this work will select a pair of search patterns based on the given system design and its application environment and optimize them accordingly. It is capable of predicting the performance including the assembled actuator and sensor and therefore improves the estimation results of the expected performance compared to existing work.

2. CubeISL SYSTEM ANALYSIS

CubeISL is a project by the German Aerospace Center (DLR) and its Institute of Communications and Navigation. The Optical Satellite Links Department, who has also developed the predecessor OSIRIS4CubeSat for the PIXL-1 mission, is in charge of designing, testing, and verifying this 1 unit payload. In Fig. 1 the acquisition scheme as developed for CubeISL is presented. This evaluation focuses on phase (a), the initial search, where no hits have yet been detected. Sketched is the slow scanning *Grid* pattern in combination with a *Spiral*.

The subsequent phases deal with the challenge that both LCTs have to precisely align themselves to each other after the acquisition hit occurred and decide when a tracking lock has been achieved. Terminals A and B are only distinguished by their transmit and receive wavelengths and are interchangeable in software terms, allowing both to operate as a terminal for pointing, acquisition, and tracking (T-PAT) or terminal for detection, adjustment, and tracking (T-DAT), which determines their behavior during acquisition. As the actual switching to tracking mode presents its own challenges, it should be noted that closed-loop control is part of ongoing work. The defined set of system parameters defines the specific challenges of the envisaged optical ISL. The scenario in this work is closely related to the CubeISL project. This 1U optical payload inside a 6U CubeSat, shown in Fig. 2, is designed to establish an ISL of up to 1500 km between two low earth orbit (LEO) satellites [8]. The ADCS system of the satellite is coupled to the optical system via the aperture of the system due to the attitude with respect to the link partner. In CubeISL, the transmit (TX) path is coupled with the receive (RX) path via the FSM. The quadrant photo detector (QPD) features two independent evaluation electronics, which can detect either
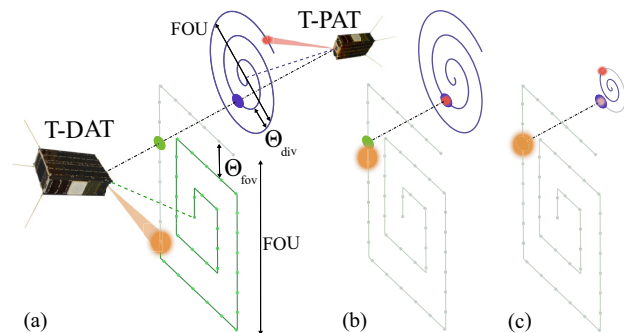

Fig. 1. Brief sequence of the acquisition scheme with (a) searching for an initial hit. (b) Step-wise adjustments of T-DAT by reoccurring hits from T-PAT. (c) T-DAT is aligned within the accuracy of its divergence angle Θ_{div}, waiting for T-PAT to acquire (indicated with gray spiral).
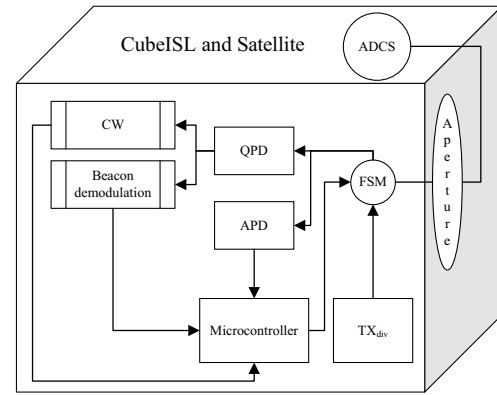

Fig. 2. Schematic of the interdependencies between components in the system, consisting of CubeISL and the 6U CubeSat attitude determination and control system (ADCS).

Table 1. Summary of the Simulated FOV at Percentages of Total to Received Signal Power, Using Optical Design Software

Cases	100%, mrad	50%, mrad	0%, mrad
1553 nm (QPD) FSM centered	0.664	1.326	1.990
1553 nm (QPD) FSM full + stroke	0.350	1.220	2.094
1553 nm (QPD) FSM full—stroke	0.488	1.222	2.130
1590 nm (QPD) FSM centered	1.048	1.326	1.906
1553 nm (APD) FSM centered	1.920	n/a	n/a

continuous wave (CW) or modulated beacon signals. A major design parameter is the field of view (FOV) of the terminal. This parameter is defined in the literature as

$$2 \cdot \arctan \left(0.5 \cdot \text{sensor size} \cdot \text{focal length}^{-1} \right) \quad \textbf{(1)}$$

for the chief ray. In contrast, the real system might include beam truncation or deformation effects within its optical system. CubeISL operates at 1590 nm in direct to earth (DTE) and either 1553 nm or 1536 nm in ISL. Therefore, Table 1 shows the FOV of the CubeISL system using different definitions related to the received power. The cases are defined by the percentage of power of the full spot received by the QPD tracking sensor or the avalanche photo diode (APD) data sensor. It has been decided to use the 50% value at the FSM center position for the QPD as the nominal case, as it shows the best overlap in the involved wavelength configurations. However, based on the link budget [8], values of more than 0% and up to 100% would be feasible and could therefore have a significant impact on the subsequent acquisition process, as the FOV range between columns one and three implies.

A condensed set of parameters with high impact on the scenario is summarized below in Table 2. All standard deviations are given as 3σ. The field of uncertainty (FOU) is considered to be the angular radius of the maximum uncertainty from

Table 2.   Scenario Parameters of the Used CubeISL Scenario Using Two CubeSats

Symbol	Value	Unit
Θ_{div}	$192.8 \cdot 10^{-6}$	rad
Θ_{QPD}	$1.326 \cdot 10^{-3}$	rad
BW_{QPD}	200	Hz
BW_{QPDCW}	$1.59 \cdot 10^{3}$	Hz
Θ_{APD}	$1.935 \cdot 10^{-3}$	rad
BW_{APD}	$3.5 \cdot 10^{3}$	Hz
BW_{FSM}	72	Hz
f_R	280	Hz
$3\sigma_{\text{FOU}}$	[0.1, 0.2, 0.3, 0.4, 0.5]	deg
$3\sigma_{\text{vib}}$	$10 \cdot 10^{-6}$	rad
$3\sigma_{\text{drift}}$	0.08	deg/s
t_{lim}	[60, 600]	s
t_a	0.002	s
p	1600	—
t_s	0.001	s

the actual target. This range is limited to ± 1 deg due to the design of the optical system. For the ISL case, only a subset of the FOU has been considered, as shown later in Figs. 6 and 7, where exponentially increasing search times are expected to exceed the time limit t_{lim} and thus the power budget of the mission. Therefore, if a link in CubeISL is not established within 10 min, the acquisition is cancelled and the satellite is reorientated to recharge the batteries. A new attempt can be made thereafter.

The divergence Θ_{div} and the FOV Θ_{fov} are design parameters of CubeISL and play a decisive role in the results of the analysis. Since the simulation shall lead to a direct result for experimental tests, it is important to use the parameters from the LCT. In Table 2 are two bandwidths mentioned for the QPD. This is due to the fact that the electronics are able to perform beaconless acquisition with CW and superimposed data as well as with a dedicated beacon with 10 kHz modulation (cf. Fig. 2). The latter is particularly useful in scenarios with power fades due to atmospheric effects in DTE links [9]. The demodulation electronics provide a bandwidth of 200 Hz for the modulated channel and 1.59 kHz for the CW channel without additional signal processing. Furthermore, the ability of the data receiver to support the acquisition is investigated in the simulation. The advantages of using an APD as the acquisition sensor are the FOV obtained in this design and the higher bandwidth based on an estimate from preliminary tests. The disadvantage of using the data sensor for acquisition is due to the APD itself not being able to provide information about the location of a hit. However, the deflection of the FSM can be used as a reference to determine the angular offset in the event of a valid signal. The vibrations introduced are a combination of attitude control jitter and micro-vibrations. The drift results from the limited precision of the satellite's control system, which causes it to tumble around the target position. The motion is not necessarily Gaussian distributed as it depends on the active closed loop control. The maximum time limit t_{lim} before an acquisition is aborted is 600 s. After this time it is assumed that the satellite bus batteries need to be recharged and are no longer available for terminal operation.

3. OPTICAL INTER-SATELLITE ACQUISITION SIMULATION

A Monte Carlo simulation has been chosen as the analysis tool because this work involves randomly distributed disturbances that could only be tested at great expense on a hardware breadboard. In addition, this simulation will be nested within a tool that takes characteristic link parameters as input and optimizes selected pattern combinations in terms of their probability of success and mean acquisition time (MAT).

A. Bandwidth Considerations for the Actuator and Sensor

Well-known functions are used to generate the search patterns for the evaluation [1]. The frequently used patterns *Spiral* and *Grid* are often used due to their simple implementation. The patterns *Rose* and *Lissajous* result from the superposition of trigonometric functions. The advantage is that these patterns can be operated much more efficiently in terms of power consumption [10]. In addition, they enable faster period durations for a cycle, compared to quasi-static (point-to-point) control, control by exploiting the resonant frequency of the actuators. This leads to the conclusion that it is of high importance to consider the hardware characteristics of the actuator and sensor devices. The integrated micro-electro-mechanical system (MEMS) FSM does not feature an internal position control sensor, which would improve the steering capabilities. Nevertheless, multiple options for open-loop control are available [11]. The FSM is modeled as a second-order system including an upstream first-order low-pass filter with a 72 Hz cutoff frequency, which can be disabled for resonant operation.

For the acquisition sensor, three configurations are considered as mentioned in Table 2. The sensors themselves are represented as first-order low-pass filters with corresponding cutoff frequency. In the application, a recognized hit will depend, among other things, on additional conditions. For example, the position of the hit on the aperture plays a role, as does the requirement that the signal is actually sampled during a hit. However, since the latter is a question of implementation, which can also be interrupt-based and is always assumed to occur with at least 50% power, a simplification can be made. The maximum possible event duration of a hit is determined from the angular velocity of the transmitting ω_{TX} and receiving ω_{RX} terminals, together with any disturbance $\Delta\omega$. The minimum result $\min(t_{\text{TX}}, t_{\text{RX}})$ of Eqs. (2) and (3) indicates how fast the sensor must react to the signal in order to detect it:

$$t_{\text{TX}} = \frac{\Theta_{\text{div}}}{\underbrace{\omega_{\text{TX}} + \Delta\omega_{\text{TX}}}_{\omega_A}} \geq BW_{\text{sensor}_A}^{-1} \Rightarrow v_A, \tag{2}$$

$$t_{\text{RX}} = \frac{\Theta_{\text{fov}}}{\underbrace{\omega_{\text{RX}} + \Delta\omega_{\text{RX}}}_{\omega_B}} \geq BW_{\text{sensor}_A}^{-1} \Rightarrow v_B. \tag{3}$$

If this simplification is pursued further, a maximum permissible angular velocity v can be derived, which differentiates between the perspective of each terminal. For reasons of clarity, they are referred to below as either terminal A or terminal B

and are limited by the sensor device used. ν_A and ν_B state the limiting angular velocity for an opposing static counterpart. One can therefore derive the maximum allowed angular velocity of one terminal, taking into account its angular velocity as calculated in Eqs. (4) and (5):

$$\omega_{A_{\max}} = \nu_A - \omega_B \cdot \nu_A \cdot \nu_B^{-1}, \tag{4}$$

$$\omega_{B_{\max}} = \nu_B - \omega_A \cdot \nu_B \cdot \nu_A^{-1}. \tag{5}$$

This also means that, in principle, noise can be beneficial because it artificially increases the velocity of the pattern. However, this holds only true at first glance. In general, it is desirable to achieve the maximum velocity through controlled manipulation, not through interference, as this would otherwise result in less accurate position information. The same statement can be made about the drift error. When a hit occurs and it is detected by the sensor while the drift rate is too high, the counter terminal will have already disappeared from the FOV before the next potential signal event. Therefore, a maximum allowable untracked drift rate can be calculated as

$$\Delta\omega_{\max} = \frac{\Theta_{\text{fov}}/2}{T_{\text{pattern}}}. \tag{6}$$

It includes the combination of jitter due to vibrations and due to knowledge of the attitude within a reference frame, which is not dependent on the sensor bandwidth but on its FOV. Improvements can be made by better knowledge of the attitude on the satellite or LCT and by local closed-loop control of the FSM by link independent angular measurements during acquisition.

B. Optimization Framework for Patterns and the Acquisition Phase

The implemented optimization framework (see Fig. 3) considers predefined hardware design parameters of the LCT, such as the following:

- actuation sampling time (fixed pattern) t_a;
- pattern resolution p;
- actuator bandwidth BW_a;
- controller signal sampling time t_s;
- design and environment Θ_{div}, Θ_{fov}, σ_{FOU}, σ_{vib}, and σ_{drift};
- sensor bandwidth BW_s and variables that can be adapted to reach the desired performance;
- actuation sampling time (optimization pattern) α;
- pattern resolution and amplitude factors β and δ; and
- optimization weighting factors $\gamma_{1,\_,4}$ and γ_{α_1} and γ_{α_2}.

The optimization in Fig. 3 starts by generating the trajectory Tr, which is bounded by the resolution p, which also defines the time period $T_{\text{pattern}} = t_a \cdot p$ for one full scan. The pattern is scaled in amplitude and resolution using the variables β and δ. In the second step, dynamics are introduced by using the transfer function of the used actuator A. Its bandwidth BW_a and the current actuation time α determine the actual trajectory of the pattern. In the third step, the processing capabilities of the processor unit are considered. In this example, $t_s = 0.001$ s is used and therefore determines the sampling interval between
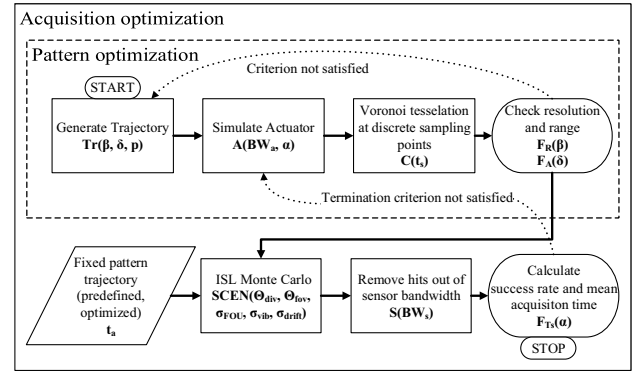

Fig. 3. Program flow chart for pattern based acquisition optimization.

two evaluation steps at which a hit can be identified by the system. As a last step in the pattern optimization routine, the two optimization parameters δ and β are used to adapt the amplitude and resolution of the pattern, taking into account the influence of the simulated actuator and the sampling interval. The metrics

$$F_A(\delta) = \left| \left(\sigma_{\text{FOU}} - \max\left(\sqrt{\text{FSM}_x(\delta)^2 + \text{FSM}_y(\delta)^2} \right) \right) \right|, \tag{7}$$

as well as

$$\begin{aligned} F_R(\beta, \delta) = \gamma_1 \cdot |\, (\Theta/2 - \text{mean}(R_{VT}(\beta))) \\ + \gamma_2 \cdot \max(\text{var}(R_{VT}(\beta))) \\ + \gamma_3 \cdot \max(Q_{VT}(\beta)) + \gamma_4 \cdot F_A(\beta, \delta), \end{aligned} \tag{8}$$

are applied to satisfy the scenario requirements with a maximum of 50 iterations and a termination tolerance of 10^{-6}. Here F_A defines the amplitude penalty based on the positions of the FSM, whereas F_R defines the resolution by the cell shapes that define the empty gaps in between the pattern trajectory. This approach is derived from a scanning trajectory optimization [12]. It has been adapted to this use case to have a comparable metric, enabling an automated design process over all patterns.

In the following second part of the optimization, both patterns are considered in combination for the acquisition process. In this simulation, the pattern for T-PAT is optimized for the resolution of the divergence, whereas the pattern for T-DAT is optimized for the FOV range in order to exploit the scanning resolution margin. The fixed pattern was optimized in the same way as described above, except that the actuation time $\alpha = t_a$ is fixed. A Monte Carlo program, based on previous work [13], helps find an approximation with 1000 randomly evaluated scenario variations for this analysis. Within this simulation the ISL scan pattern is run with perturbations applied at each evaluation point. The resulting attitude error with respect to perfect alignment is given by ϕ. A successful acquisition hit is therefore determined by

$$(\phi_A \leq \Theta_{\text{fov}} \vee \phi_B \leq \Theta_{\text{div}}) \wedge (\phi_A \leq \Theta_{\text{div}} \vee \phi_B \leq \Theta_{\text{fov}}), \tag{9}$$

which applies design parameters from the scenario definition $\text{SCEN}(\Theta_{\text{div}}, \Theta_{\text{fov}}, \sigma_{\text{FOU}}, \sigma_{\text{vib}}, \sigma_{\text{drift}})$. Over all runs, a MAT is

Table 3.   Supplementing Data for the CubeISL Scenario Parameters Using $t_a = 0.002$

Sensor	v_a $\frac{\text{rad}}{\text{s}}$	v_b $\frac{\text{rad}}{\text{s}}$	$\Delta\omega_{\max} \frac{\text{rad}}{\text{s}}$		
			$T = 3.2$ s	$T = 16.0$ s	$T = 30.2$ s
QPD_{MOD}	0.04	0.27	$2.1 \cdot 10^{-4}$	$4.1 \cdot 10^{-5}$	$2.2 \cdot 10^{-5}$
QPD_{CW}	0.31	2.11	$2.1 \cdot 10^{-4}$	$4.1 \cdot 10^{-5}$	$2.2 \cdot 10^{-5}$
APD	0.67	6.77	$3.0 \cdot 10^{-4}$	$6.0 \cdot 10^{-5}$	$3.2 \cdot 10^{-5}$

derived with corresponding success rate *SR*. The angular velocities ω_{TX} and ω_{RX} are calculated accordingly at each potential hit event. As a last processing step, recorded events outside the selected sensor S bandwidth are removed by comparing them to the maximum rates from Eqs. (2) and (3). For the evaluation of the top level optimization

$$F_{T\tilde{s}}(\alpha) = \gamma_{\alpha_1} \cdot \text{MAT} \cdot t_{\lim}^{-1} + \gamma_{\alpha_2} \cdot SR^{-1} \qquad (10)$$

is minimized as an objective function in this work. A maximum of 20 iterations is set as a limit with a termination tolerance of 10^{-4}. The MAT is divided by the maximum allowed acquisition time $t_{\lim}$, and the reciprocal of the success rate is used, so that both terms reach their minimum in the optimal configuration. The γ_{α} parameters can be used to fine-tune the results. The success rate increases exponentially while the MAT increases linearly, thus emphasizing the success criterion. Alternatively, Eq. (11),

$$F_{T\tilde{s}}^{\text{equal}}(\alpha) = \gamma_{\alpha_1} \cdot \left(1 - \text{MAT} \cdot t_{\lim}^{-1}\right)^{-1} + \gamma_{\alpha_2} \cdot SR^{-1}, \qquad (11)$$

can be used if both performance parameters are to scale equally.

4. ANALYSIS ON THE INFLUENCE OF DYNAMICS

Before the influence of the individual pattern combinations is considered, bandwidth-dependent properties will be described in more detail. For the sake of clarity, a set of unoptimized patterns is used to show the influence of the sensor choice.

A. Evaluation of Bandwidth Specific Results

In the following, Table 3 is used to display all static velocity variables that will be used in the analysis. They are determined by Eqs. (2), (3), and (6). The values for v assume a static counterpart. Variable angular velocity limits ω are displayed in Fig. 4. Since the baseline pattern uses an actuation time t_a of 0.002 s, the resulting period T equals 3.2 s. As the results in Table 4 show, the counter pattern uses five or ten times this actuation time and is therefore also calculated.

The QPD_{MOD} and APD sensor bandwidths, as referred to in Fig. 4, are used to evaluate limits of the angular velocity. Furthermore, the areas in which a possibility of acquisition exists are sketched following Eqs. (4) and (5). That excerpt demonstrates that not every hit ultimately means that it can be perceived by the acquisition sensor. It is not only important that the mean lies within these limits, but also that the majority of the extremes can be detected as well. For this reason it is important to trim both patterns in relation to each other.
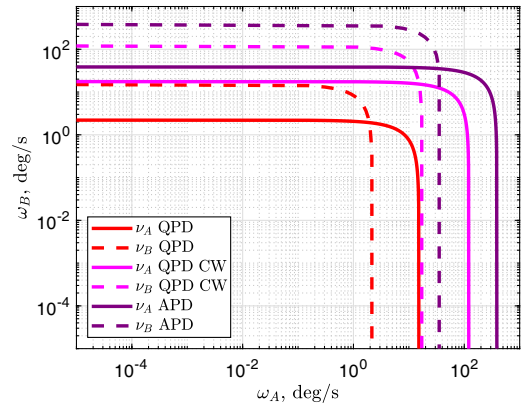
Fig. 4. Angular rate boundaries derived from the sensor bandwidth, comparing the valid hit detection rates of the considered sensor devices.

Table 4.   Ranking of the Three Best Combinations by Sensor Configuration for FOU ±0.2 deg with $\gamma_{\alpha_1} = 10$ and $\gamma_{\alpha_2} = 0.5$ for SR > 66% and $t_{\lim} = 60$ s

Sensor	α / t_{act}	F	Pattern	SR,%	MAT,s
APD	10	0.0327	Liss–rose	98.9	1.66
APD	10	0.0407	Spir–rose	99.9	2.14
APD	5	0.0667	Rose–liss	99.0	3.70
QPD_{CW}	10	0.0512	Spir–rose	96.0	2.76
QPD_{CW}	8	0.0768	Liss–rose	98.0	4.30
QPD_{CW}	8	0.1054	Liss–liss	85.1	5.97
QPD_{MOD}	5	0.0771	Liss–rose	82.3	4.26
QPD_{MOD}	10	0.1847	Spir–rose	82.6	10.72

Given that the bandwidth of the sensor system has been considered, it makes sense to investigate, in the second limiting element, the actuator system. As shown in the optimization overview, each pattern is first optimized in isolation using the defined metrics. In the global loop, however, the period of the two patterns is modified with respect to each other. In the geometry optimization concerning resolution and amplitude of the individual patterns, an underlying model of the actuator is used to capture its dynamics and limitations. Both processes can be seen in Fig. 5. The fundamental actuation time t_a does constrain the tunable actuation time to $\alpha \in \,]t_a; \, t_{\lim}/p\,]$. As a final result, for the considered example case of a *spiral–spiral* configuration, an indication of pattern period ratio influence on the performance of function F can be observed. For illustration, the difference of results between the bandwidths of the sensor-limited observation (marked as x) and an ideal sensor (marked as o) is plotted.

B. Performance Analysis of Optimized Combinations of Patterns

After the influence of the bandwidth on the results has been examined, the comparison of different pattern combinations will be performed. Two patterns make use of the resonance frequency f_R, which is a consequence of the FSM dynamics. Four types of patterns are distinguished: *Spiral*, *Grid*, *Lissajous*, and *Rose*, with
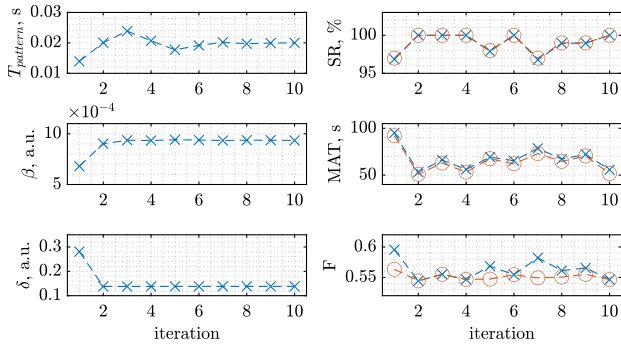
Fig. 5. Ten iterations of the optimization showing the course of the process for *spiral–spiral* using QPD$_{CW}$ and ± 0.2 deg. Depiction of the tunable variables in the left column and depiction of the metrics including objective function F in the right column.

$$x_{\text{spir}}(\Phi) = \text{FOU} \cdot \delta \cdot \frac{\Phi}{p} \cdot \cos\left(2\pi \cdot \text{FOU} \cdot \frac{\delta}{\beta} \cdot \frac{\Phi}{p}\right), \quad \textbf{(12a)}$$

$$y_{\text{spir}}(\Phi) = \text{FOU} \cdot \delta \cdot \frac{\Phi}{p} \cdot \sin\left(2\pi \cdot \text{FOU} \cdot \frac{\delta}{\beta} \cdot \frac{\Phi}{p}\right), \quad \textbf{(12b)}$$

$$x_{\text{liss}}(\Phi) = \delta \cdot \sin\left(2\pi \cdot f_R \cdot \frac{\Phi}{p}\right), \quad \textbf{(12c)}$$

$$y_{\text{liss}}(\Phi) = \delta \cdot \sin\left(2\pi \cdot \beta \cdot \frac{\Phi}{p}\right), \quad \textbf{(12d)}$$

$$x_{\text{rose}}(\Phi) = \delta \cdot \text{FOU} \cdot \sin\left(2\pi \cdot \beta \cdot \frac{\Phi}{p}\right) \cdot \cos\left(2\pi \cdot f_R \cdot \frac{\Phi}{p}\right),$$
$$\textbf{(12e)}$$

$$y_{\text{rose}}(\Phi) = \delta \cdot \text{FOU} \cdot \sin\left(2\pi \cdot \beta \cdot \frac{\Phi}{p}\right) \cdot \sin\left(2\pi \cdot f_R \cdot \frac{\Phi}{p}\right),$$
$$\textbf{(12f)}$$

and $\Phi \in [0; \ p]$. Note, that the *Grid* pattern is not formed by a continuous function but is represented by an algorithm that separates each point by the resolution β and spirals out until it reaches the amplitude δ [7,8]. Each of them combined with itself and any other pattern would result in 16 possible combinations. Preliminary investigations have shown that the *Spiral* search pattern can be trimmed very well for amplitude and resolution. It is therefore evaluated with each of the other patterns and with itself. The *Grid* pattern is the simplest and slowest of the patterns. It is the baseline because of its simple implementation. It is only considered together with the *Spiral*, since no significant improvements are to be expected with other combinations due to its long period duration. Finally, the combinations of the resonance driven patterns are examined. The results of all relevant evaluations are shown in Fig. 6 for a maximum time t_{lim} of 600 s.

First of all, it can be stated that for an FOU of ± 0.1 deg to ± 0.2 deg all patterns show a success chance of a mutual hit of almost 100%. In particular, an FOU of ± 0.1 deg gives the best results, since it is close to the range of the given FOVs. Beyond this FOU, the patterns show a decreasing tendency. If the behavior deviates from the trend, then it is always at the expense of its MAT. This becomes clear if one looks at the
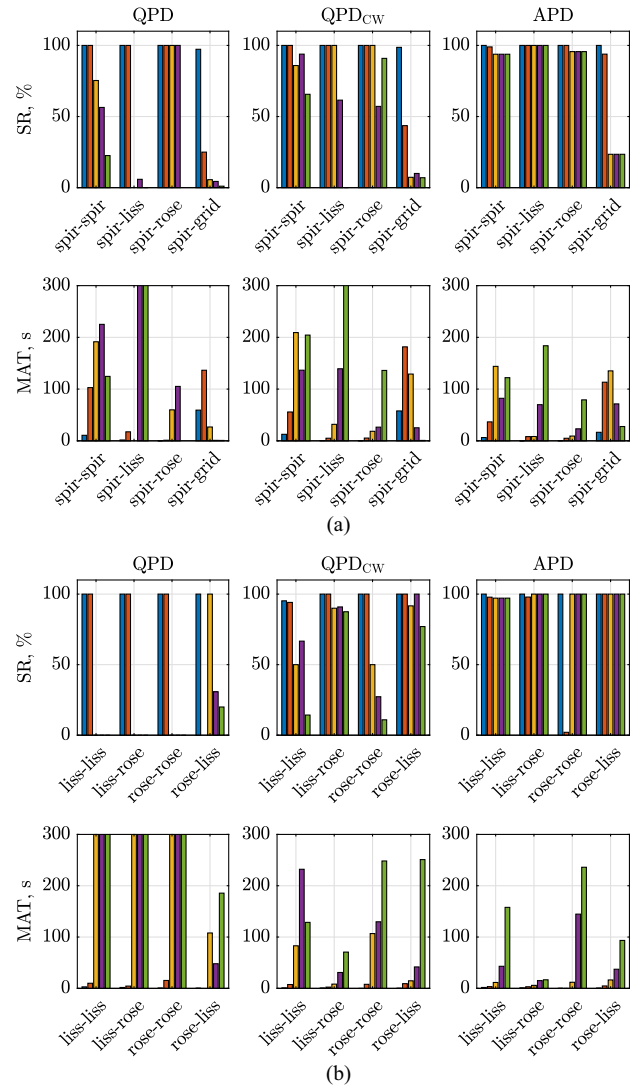

(a)

(b)

Fig. 6. Displayed are performance indicators success rate and MAT for different FOUs in ascending order [0.1 deg (blue), 0.2 deg (red), 0.3 deg (orange), 0.4 deg (purple), and 0.5 deg(green)] and a limiting search time of 600 s. (a) Spiral combinations. (b) Resonant combinations.

function value of the optimization over F. The two combinations *spiral–spiral* and *spiral–rose* show robust behavior over all sensors and all FOUs. For the resonant combinations, it is noticeable that the probability of success drops significantly above FOUs above ± 0.2 deg. This can be explained by the fact that the relative velocities increase due to expanding FOUs, while the pattern period of the fixed pattern remains constant. In the CW case, however, all combinations can show acquisitions over the whole range of FOUs, whereby the combinations *lissajous–rose* and *rose–lissajous* perform best. In general, as expected, there is a correlation between sensor bandwidth and MAT, since higher bandwidths also allow smaller periods of the patterns. As shown above, an upper limit of 600 s will result in a hit in most cases. This can then be used to align the two terminals and then switch to closed-loop tracking. At the same time, the question arises as to how a stricter requirement of 60 s will affect the acquisition when the remaining time is
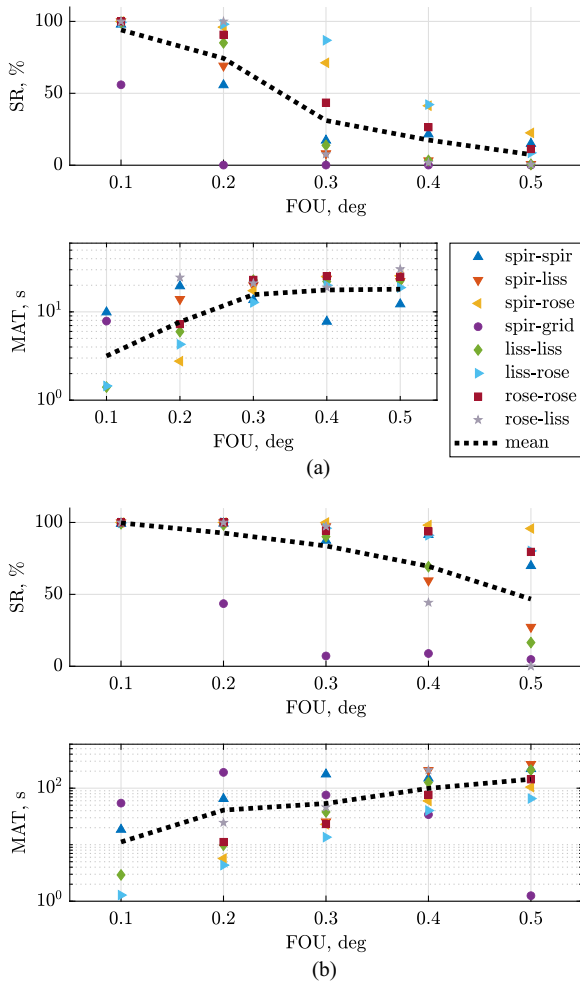
Fig. 7. Comparison of the effect on acquisition due to time limitations based on the sensor QPD$_{cw}$. (a) $t_{lim} = 60$ s and (b) $t_{lim} = 600$ s.

to be reserved for the transmission of data. Therefore, Fig. 7 presents the comparison of the two scenarios for the QPD$_{cw}$ sensor. It is noticeable that the exponential increase of the MAT in the 60 s case flattens towards the end and approaches a value of 30 s. In addition, as expected, all combinations drop earlier in their success rate. From ± 0.4 deg onwards, all combinations are already below 50%, whereas at 600 s even ± 0.5 deg can be achieved with 96%. In both scenarios, the two combinations *spiral–rose* and *lissajous–rose* seem to show the best performance. The baseline pattern is inferior in all cases.

Once the influence of t_{lim} is clearer, a detailed list (see Table 4) of the top performers for a particular FOU is generated. As previously experienced, higher bandwidth sensors will also allow for better acquisition performance. For the given scenario, the two patterns *spiral–rose* and *lissajous–rose* appear to be the most suitable. They provide low F values across sensors. The ratio 10 seems to be a good choice for this particular case. In general it would be intuitive if the ratio drops with higher bandwidth sensors. But there is another setting on the resonant pattern that can influence the velocity, namely, the drive frequencies. For the example of *lissajous–rose*, they were tuned to 236–204 Hz, 236–182 Hz, and 236–107 Hz in decreasing order of sensor bandwidth, which proves that the

tunable driving frequency is reduced. It should be noted that the MAT as defined in this paper refers to the time taken for a first hit. Based on this knowledge, additional time is required for multiple T-PAT scans to perform the final alignment steps on T-DAT for a full acquisition according to the acquisition scheme [8].

Thorough analysis of the results suggests ways to improve the optimization function F. The assumed error drift of the satellite has turned out to be one of the main influencing factors. In fact, the disturbances add to the velocity of the search pattern. For a first hit this can even be helpful, as the resulting speed of the pattern is increased, and thus by chance a larger area is traversed in less time. However, this uncontrolled movement also has the disadvantage that it does not stop after a hit [see Eq. (6)]. Therefore, the subsequent alignment phase is correspondingly more difficult. It is desirable that a position change consists only of known or measurable changes. A proposal to reduce the influence of drift is the implementation of a secondary attitude estimation algorithm on the LCT, which can partially compensate for known drift by feed-forward FSM control and is subject to ongoing work. In addition, vibrations from the satellite platform that couple into the FSM can be reduced by active closed-loop control or passive countermeasures such as dampers. The proposed optimization of the pattern combinations achieves a significant improvement compared to the baseline *spiral–grid* [7]. With a success probability of up to 99.9%, it demonstrates that an inter CubeSat optical ISL is feasible.

5. CONCLUSION

The focus of this work is on the optimization of bandwidth constrained pattern combinations for optical ISL acquisition. The actuator bandwidth is considered, as it has a significant influence on the achievable pattern period and the trajectory precision. The sensor bandwidth is used to define the required detection time and thus the permissible relative velocity of both patterns as well as applied stochastic errors. The disturbances themselves are distinguished into Gaussian distributed vibrations and error drift due to the accuracy of the satellite control. It is possible to have temporally unsynchronized patterns that start at arbitrary times and initial deflections and are still able to intersect with an assessable probability. Thereby, it is advantageous if the period of the two patterns deviates from each other. An algorithm is implemented to approximate an optimum of this ratio.

According to the results, it makes sense to choose a factor of about 10 for the period of the tuned pattern with respect to the fixed pattern if all drive frequencies remain the same. When a constant success rate is targeted, an exponential increase of the MAT is to be expected for a linearly increasing FOU. Comparing a maximum search time of 60 s and a maximum search time of 600 s, an FOU of ± 0.2 deg significantly increases the average success rate of all patterns by up to 50% points. In the same context of 60 s, the best performing combinations are *spiral–rose* and *lissajous–rose*. Depending on the choice of sensor, they can achieve success rates from 82.3% to 99.9%, with MATs for the first hit ranging from 10.72 s to 1.66 s. Hardware tests are currently being carried out to verify

the simulations and to validate the complete acquisition and tracking scheme.

REFERENCES

1. M. Scheinfeild, N. S. Kopeika, and A. Shlomi, "Acquisition time calculation and influence of vibrations for microsatellite laser communication in space," Proc. SPIE **4365**, 195–205 (2001).
2. X. Li, Q. Song, J. Ma, *et al.*, "Spatial acquisition optimization based on average acquisition time for intersatellite optical communications," in *Academic Symposium on Optoelectronics and Microelectronics Technology and 10th Chinese-Russian Symposium on Laser Physics and Laser TechnologyOptoelectronics Technology (ASOT)* (IEEE, 2010), pp. 244–248.
3. X. Li, S. Yu, J. Ma, *et al.*, "Analytical expression and optimization of spatial acquisition for intersatellite optical communications," Opt. Express **19**, 2381–2390 (2011).
4. M. S. Bashir and M.-S. Alouini, "Adaptive acquisition schemes for photon-limited free-space optical communications," IEEE Trans. Commun. **69**, 416–428 (2021).
5. L. Friederichs, U. Sterr, and D. Dallmann, "Vibration influence on hit probability during beaconless spatial acquisition," J. Lightwave Technol. **34**, 2500–2509 (2016).
6. U. Sterr, M. Gregory, and F. Heine, "Beaconless acquisition for ISL and SGL, summary of 3 years operation in space and on ground," in *International Conference on Space Optical Systems and Applications (ICSOS)* (IEEE, 2011), pp. 38–43.
7. B. Rödiger, R. Rüddenklau, C. Schmidt, *et al.*, "Acquisition concept for optical inter-satellite communication terminals on CubeSats," in *Small Satellites Systems and Services—The 4S Symposium* (2022).
8. J. R. Nonay, R. Rüddenklau, A. Sinn, *et al.*, "Horizontal free-space optical link with CubeISL over 143 km," J. Opt. Commun. Netw. **16**, 593–601 (2024).
9. "Optical communications physical layer, pink sheets," Draft Recommended Standard CCSDS 141.0-P-1.1 (The Consultative Committee for Space Data Systems (CCSDS), 2020).
10. E. Csencsics and G. Schitter, "System design and control of a resonant fast steering mirror for Lissajous-based scanning," IEEE/ASME Trans. Mechatron. **22**, 1963–1972 (2017).
11. V. Milanović, A. Kasturi, J. Yang, *et al.*, "Closed-loop control of gimbal-less MEMS mirrors for increased bandwidth in LiDAR applications," Proc. SPIE **10191**, 101910N (2017).
12. T. Tuma, J. Lygeros, A. Sebastian, *et al.*, "Optimal scan trajectories for high-speed scanning probe microscopy," in *American Control Conference (ACC)* (IEEE, 2012), pp. 3791–3796.
13. J. Ma, G. Lu, S. Yu, *et al.*, "Acquisition performance analysis for intersatellite optical communications with vibration influence*," Chin. Phys. B **29**, 014205 (2020).